Cell intrinsic mechanical regulation of plasma membrane accumulation at the cytokinetic furrow

Roberto Alonso-Matilla[1], Alice Lam[2], and Teemu P. Miettinen[3,#]

Affiliations:
[1] Department of Biomedical Engineering, University of Minnesota, Minneapolis, MN 55455, USA.
[2] Department of Electrical Engineering and Computer Science, Massachusetts Institute of Technology, Cambridge, MA 02139, USA.
[3] Koch Institute for Integrative Cancer Research, Massachusetts Institute of Technology, Cambridge, MA 02139, USA.

[#] Correspondence to: teemu@mit.edu

Keywords: Cytokinesis, plasma membrane, actomyosin, biophysical model, membrane tension

This PDF file includes:
Main Text
Figures 1 to 5

Supplementary files include:
Supplementary Notes 1-3
Supplementary Table S1
Supplementary Figures S1-S12
Supplementary Movies S1-S5

ABSTRACT

Cytokinesis is the process where the mother cell's cytoplasm separates into daughter cells. This is driven by an actomyosin contractile ring that produces cortical contractility and drives cleavage furrow ingression, resulting in the formation of a thin intercellular bridge. While cytoskeletal reorganization during cytokinesis has been extensively studied, little is known about the spatiotemporal dynamics of the plasma membrane. Here, we image and model plasma membrane lipid and protein dynamics on the cell surface during leukemia cell cytokinesis. We reveal an extensive accumulation and folding of plasma membrane at the cleavage furrow and the intercellular bridge, accompanied by a depletion and unfolding of plasma membrane at the cell poles. These membrane dynamics are caused by two actomyosin-driven biophysical mechanisms: the radial constriction of the cleavage furrow causes local compression of the apparent cell surface area and accumulation of the plasma membrane at the furrow, while actomyosin cortical flows drag the plasma membrane towards the cell division plane as the furrow ingresses. The magnitude of these effects depends on the plasma membrane fluidity and cortex adhesion. Overall, our work reveals cell intrinsic mechanical regulation of plasma membrane accumulation at the cleavage furrow that generates localized membrane tension differences across the cytokinetic cell. This may locally alter endocytosis, exocytosis and mechanotransduction, while also serving as a self-protecting mechanism against cytokinesis failures that arise from high membrane tension at the intercellular bridge.

MAIN TEXT

Cytokinesis, the process of partitioning a mother cell's cytoplasm into daughter cells, is an essential step in the completion of the cell division cycle. The key biomechanical forces responsible for animal cell cytokinesis are generated by the actomyosin cortex, a network of myosin-II motors and crosslinked actin filaments (1). A localized increase in actomyosin contractility at the cell's equatorial region, coupled with actomyosin relaxation at the cell poles generates a cortical contractility gradient that induces the movement of cortical material from the cell poles towards the equator (2, 3). At the cell's equator, an actomyosin ring assembles, constricts, and forms a cleavage furrow, an indentation of the cell's surface. The cleavage furrow, also known as the cytokinetic furrow, advances inwards until the daughter cells are only connected by a narrow intercellular bridge (4–6). These early stages of cytokinesis, which typically last only ~10 min, are then followed by the formation of the midbody, reorganization of the cytoskeleton and eventually the final abscission of the intercellular bridge (5–7).

Cytokinetic fidelity is critical for maintaining cell fitness and tissue homeostasis, and for preventing cancer initiation and progression (8). Errors in cytokinesis can lead to imperfect partitioning of cellular components, and a failed cytokinesis will result in polyploidy or cell death. A successful completion of cytokinesis depends on the mechanical forces within the intercellular bridge. High tension in the intercellular bridge inhibits or delays cell abscission by hindering proper assembly and function of the abscission machinery. This is mediated, at least in part, by tension in the plasma membrane (7, 9–13), suggesting that cytokinetic fidelity would benefit from accumulation of plasma membrane at the cytokinetic furrow. However, while extensive efforts have been dedicated to study cytoskeletal organization and cell signaling during cytokinesis, (reviewed in (2–6)), significantly less is known about cytokinetic plasma membrane dynamics and the mechanisms impacting these dynamics (14).

The plasma membrane is a highly folded and fluidic structure that is predominantly composed of proteins (~50%) and lipids (~50%), and that attaches to the actin cortex by membrane-cortex linker proteins (15). Several studies have shown that certain plasma membrane proteins and lipids accumulate at the cytokinetic furrow during cytokinesis. For example, caveolin-1, a key protein forming membrane reservoirs called caveolae, as well as several

phosphoinositides, which also have a major role in regulating cytokinesis, accumulate at the cytokinetic furrow (9, 16–20). Although some plasma membrane components accumulate at the cytokinetic furrow, it remains unclear as to what extent the accumulation of specific membrane components reflects the overall dynamics of the plasma membrane. Consequently, it is essential to gain a deeper understanding of how cytoskeletal forces regulate plasma membrane movement and tension at the cleavage furrow and intercellular bridge.

Here, we carry out live cell imaging and biophysical modeling of plasma membrane dynamics during leukemia cell cytokinesis. We discover that the plasma membrane accumulates at the cytokinetic furrow, and we reveal two cell-intrinsic biophysical mechanisms responsible for this behavior. Our results show that cytoskeletal mechanisms driving cell division also act to decrease membrane tension at the cleavage furrow and intercellular bridge, thereby assisting in the completion of cytokinesis.

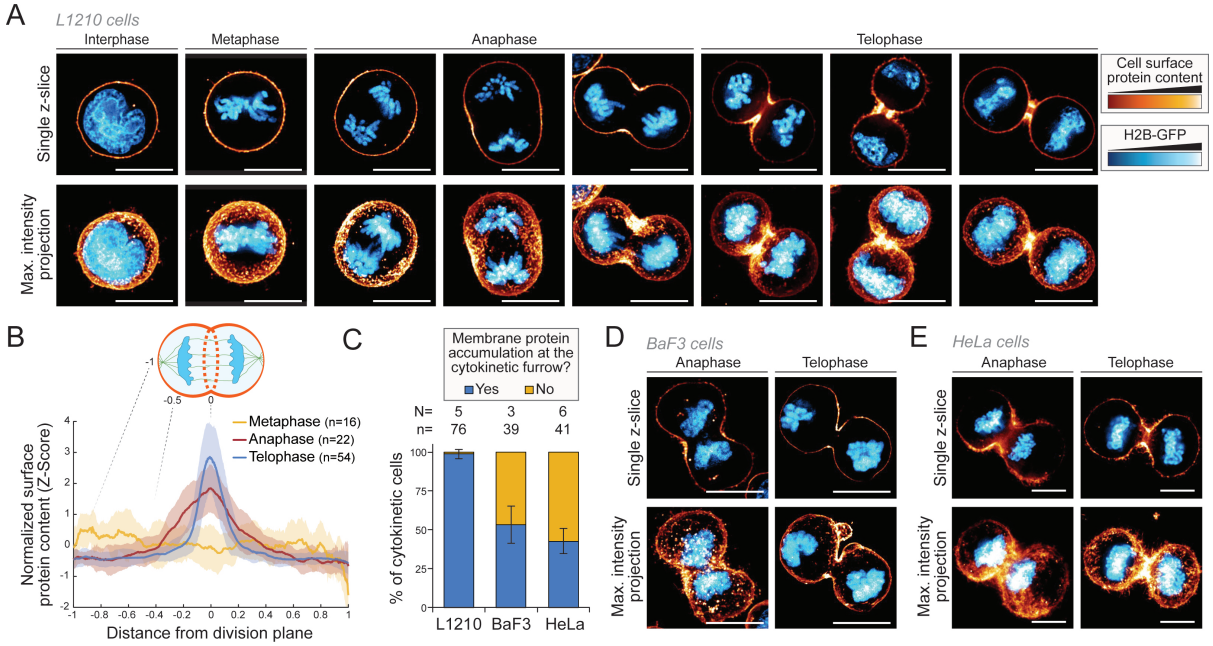

Figure 1. Cell surface proteins accumulate at the cytokinetic furrow and intercellular bridge.
(A) Representative images of mitotic and cytokinetic L1210 cells expressing H2B-GFP (blue, DNA) and labeled for cell surface protein content (orange/yellow). Cells were imaged immediately after labeling. Each image is a separate cell. **(B)** Quantifications of cell surface protein content as a function of distance from the division plane, as indicated in the schematic on top. Lines and shaded areas depict mean±SD, n depicts the number of individual cells in each cell cycle stage. **(C)** Percentage of cytokinetic cells that exhibit the accumulation of plasma membrane proteins at the cleavage furrow in the indicated cell lines. Data depicts mean±SD of independent experiments. N depicts the number of independent experiments and n depicts the total number of cytokinetic cells. **(D, E)** Representative images of cytokinetic BaF3 (D) and Hela (E) cells expressing H2B-GFP (blue) and labeled for cell surface protein content (orange/yellow). Scale bars denote 10 µm.

RESULTS

Global accumulation of plasma membrane proteins at the cleavage furrow and intercellular bridge

We sought to study how cell-intrinsic factors regulate plasma membrane movement on the cell surface. We labelled all plasma membrane proteins accessible on the external side of the cell using an amine-reactive, cell-impermeable, fluorescent label. As a model system, we used suspension grown mouse lymphocytic leukemia cell line, L1210, that expressed histone H2B fused with green fluorescent protein (H2B-GFP) to visualize DNA. These cells are

spherical and display little to no attachment to the growth substrate or neighboring cells. The membrane protein labeling revealed that cells in interphase and early mitosis (prophase to metaphase) displayed an even distribution of plasma membrane proteins on all sides of the cell (Fig. 1A). However, during early cytokinesis, the plasma membrane protein content polarized, with proteins accumulating at the cytokinetic furrow (Fig. 1A). This membrane protein accumulation was initially evident in anaphase cells, coinciding with the onset of cleavage furrow constriction, and the protein accumulation increased with the progression of cytokinesis (Fig. 1B, Fig. S1). Later in cytokinesis, membrane protein accumulation was predominantly observed in the intercellular bridge (Fig. 1A, B). Similar membrane protein dynamics were seen across all L1210 cells imaged (Fig. 1C).

We verified that our results are not specific to our approach for labeling cell surface proteins by using a thiol-reactive, cell impermeable, fluorescent label. This labeling revealed similar plasma membrane protein accumulation at the cytokinetic furrow as observed with the amine-reactive label (Fig. S2). Then, to ensure that these plasma membrane protein dynamics were not limited to a single cell type, we imaged a suspension grown mouse pro-B cell myeloma cell line (BaF3), and an adherent human adenocarcinoma cell line (HeLa). Both cell lines displayed an accumulation of plasma membrane proteins at the cleavage furrow (Fig. 1D, E), although this effect was not uniform across cells (Fig. 1C). From here on, we investigated plasma membrane dynamics using L1210 cells as our primary model system.

Plasma membrane folds at the cleavage furrow and unfolds at the cell poles

We considered two hypothetical models of plasma membrane composition and structure that could explain the high membrane protein content at the cleavage furrow (Fig. 2A). In model 1, the surface density of proteins, i.e., the number of proteins per unit of membrane area, at the cleavage furrow increases. In this model, plasma membrane lipids do not accumulate at the furrow. In model 2, the surface density of proteins remains constant, and plasma membrane area increases at the furrow due to membrane folding (Fig. 2A). This would result in plasma membrane lipids, carbohydrates, and other membrane components displaying a higher density at the furrow. Importantly, in model 2, plasma membrane accumulation at the cleavage furrow predicts a local decrease in membrane tension at the furrow, whereas model 1 would not result in significant membrane tension changes at the furrow.

To distinguish these two models, we first labelled the membrane lipids of live L1210 cells with a CellMask plasma membrane stain. This revealed that plasma membrane lipids accumulate at the cytokinetic furrow and the intercellular bridge (Fig. 2B). Then, we labeled live cell plasma membrane using wheat germ agglutinin (WGA), which binds carbohydrates on glycoproteins and glycolipids. WGA labeling accumulated to the cytokinetic furrow and intercellular bridge (Fig. 2C). We also labelled plasma membrane cholesterol in fixed cells using Filipin III, which revealed cholesterol accumulation at the cytokinetic furrow, especially in later stages of cytokinesis (Fig. 2D). With all three approaches, we observed that plasma membrane was distributed evenly on all sides of the cell prior to cytokinesis. Overall, these results support our model 2 (Fig. 2A), wherein the plasma membrane protein accumulation at the cytokinetic furrow is attributed to a local increase in cell surface area (i.e., membrane folding).

To verify that plasma membrane reservoirs accumulate at the cytokinetic furrow, we imaged L1210 cells using scanning electron microscopy (SEM). We observed that the plasma membrane at the cytokinetic furrow displays significantly greater structural complexity and membrane folds compared to the membrane observed at the cell poles (Fig. 2E). This difference was particularly pronounced during early cytokinesis, where the cytokinetic furrow and intercellular bridge displayed large membrane folds. This membrane accumulation was specific to cytokinesis, as cells arrested in prometaphase by the kinesin inhibitor S-trityl-l-cysteine (STLC) displayed uniform membrane folding on all sides of the cell (Fig. S3A). As the cytokinetic furrow fully closed, the membrane accumulation became undetectable in SEM images (Fig. 2E). Overall, these results confirm that the plasma membrane as a whole, and not just particular membrane components, accumulates in the cytokinetic furrow.

Consequently, our results suggest the existence of membrane tension gradients between the cell equator (low tension) and cell poles (high tension) during cytokinesis.

We also carried out SEM imaging of plasma membrane structure in cytokinetic BaF3 cells. These cells also displayed additional membrane folding at the cleavage furrow (Fig. S3B). However, membrane accumulation at the cleavage furrow was not present in every BaF3 cell, and overall, the BaF3 cells displayed a more diverse membrane structure compared to L1210 cells.

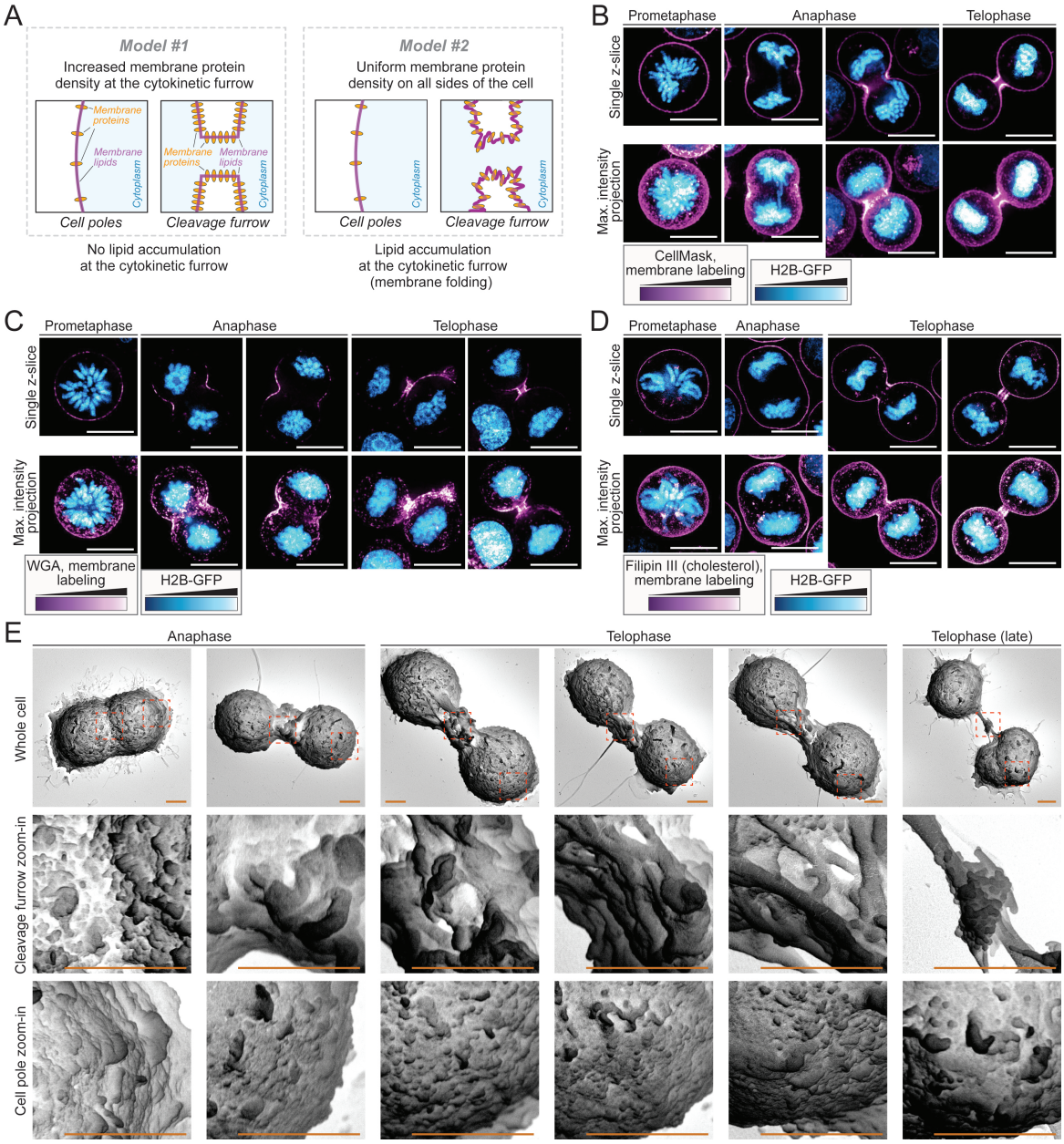

Figure 2. Excess plasma membrane accumulates at the cytokinetic furrow and depletes at the cell poles. **(A)** Two competing models that can explain the accumulation of plasma membrane proteins at the cytokinetic furrow. **(B-D)** Representative images of mitotic and cytokinetic L1210 cells expressing H2B-GFP (blue, DNA) and labeled for plasma membrane (purple/white) using CellMask (panel B, N=3 independent experiments, n=46 cytokinetic cells), WGA (panel C, N=2 independent experiments, n=31 cytokinetic cells), or Filipin III (panel D, N=3 independent experiments, n=68 cytokinetic cells). Scale bars denote 10 µm. **(E)** Representative SEM images of fixed L1210 cells in cytokinesis. N=3 independent experiments, n=45 cytokinetic cells. Scale bars denote 2 µm.

Null models for the biophysical basis of plasma membrane dynamics during cytokinesis

We then investigated the biophysical mechanism(s) responsible for membrane accumulation at the cytokinetic furrow. We considered three potential mechanisms that can cause local membrane accumulation (or depletion): First, actomyosin driven changes in cell shape during cytokinesis can locally alter the apparent cell surface area which could influence plasma membrane accumulation (Fig. 3A). Second, cortical flows, driven by cortical contractility gradients, are directed towards the cell division plane (2, 3), and membrane-cortex drag forces (21–25) could pull the plasma membrane towards the cleavage furrow (20, 23, 26) (Fig. 3A). Third, endocytosis and exocytosis can locally decrease and increase plasma membrane content, respectively. If exocytosis is localized to the cleavage furrow and endocytosis to the cell poles during early cytokinesis, then this membrane trafficking could increase plasma membrane area at the furrow (Fig. 3A). These three mechanisms are not mutually exclusive, and each of them could cause plasma membrane to accumulate at the cytokinetic furrow while depleting plasma membrane at the cell poles, as observed in our experiments.

Plasma membrane accumulation at the cleavage furrow is caused by movement of plasma membrane reservoirs on the cell surface

To identify the biophysical mechanism(s) responsible for plasma membrane accumulation at the cytokinetic furrow, we first examined if the membrane accumulation can be explained by the movement of plasma membrane on the

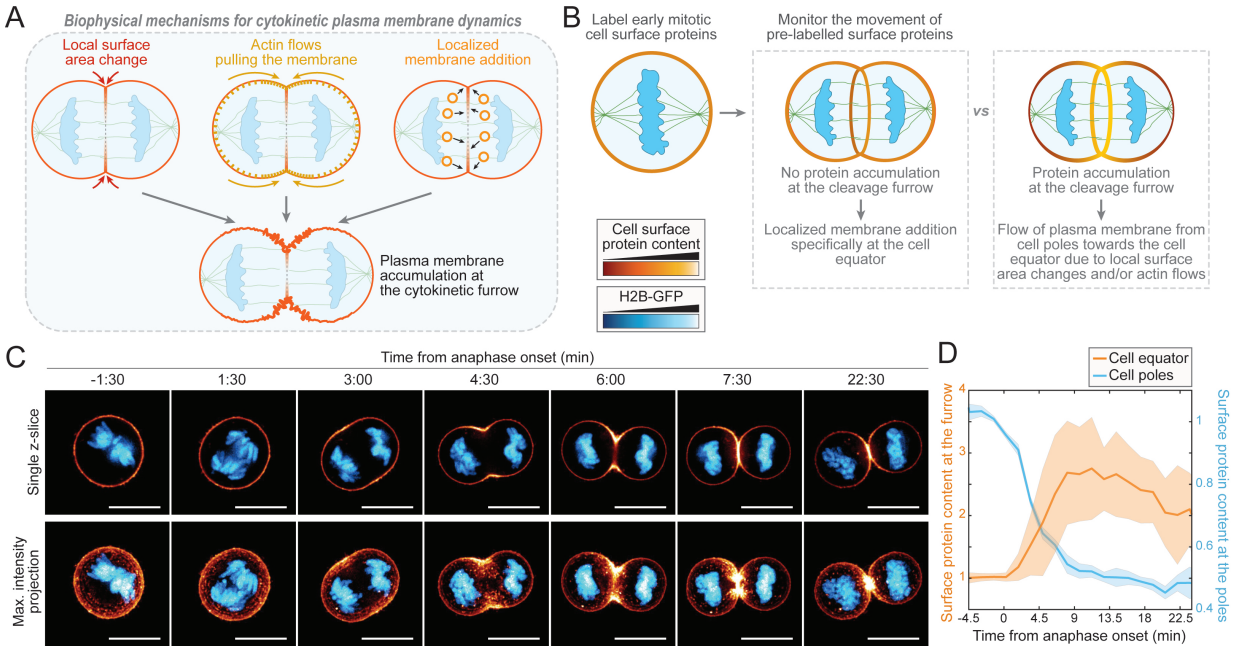

Figure 3. Plasma membrane accumulation at the cleavage furrow is caused by movement of plasma membrane reservoirs on cell surface.

(A) Three mutually non-exclusive biophysical processes that can explain the plasma membrane accumulation at the cytokinetic furrow. **(B)** The experimental setup: Pre-labelled plasma membrane proteins are imaged over time to examine whether the pre-labelled proteins accumulate at the cytokinetic furrow, indicative of membrane movement on the cell surface. Since internal membranes are not labelled, exocytosis-driven membrane accumulation will not result in a detectable signal accumulation. **(C)** Representative timelapse imaging of L1210 cells expressing H2B-GFP and labeled for cell surface protein content (orange/yellow). Scale bars denote 10 µm. **(D)** Quantifications of L1210 cell surface protein content at the cytokinetic furrow (orange) and cell poles (blue) as a function of time from anaphase onset. Lines and shaded areas depict mean±SD (N=3 independent experiments, n=14 cells). Data is normalized to the average of values at t≤0.

cell surface or if exocytosis is required. We labelled plasma membrane surface proteins in early mitosis and tracked these pre-labelled surface proteins (Fig. 3B). If plasma membrane accumulation at the cleavage furrow is driven primarily by localized insertion of internal vesicles, i.e., exocytosis, we would not observe membrane accumulation, as the newly added membrane was not pre-labelled. However, if the plasma membrane accumulation is primarily driven by membrane movement on the cell surface, then we should observe the pre-labelled membrane accumulate at the furrow (Fig. 3B). Live cell imaging of both L1210 and HeLa cells indicated that the pre-labelled membrane proteins accumulate at the cleavage furrow and deplete at the cell poles as cytokinesis progresses (Fig. 3C, Fig S4, Movie S1). In L1210 cells, the surface protein accumulation at the cleavage furrow reached its maximum within 10 minutes of cytokinesis, as the furrow ingression completed (Fig. 3D). In later cytokinesis, the surface protein accumulation slowly dissipated. Intracellular fluorescence signals remained consistently low throughout the timelapse imaging, especially in L1210 cells, indicating minimal endocytosis of the labelled plasma membrane proteins. Thus, plasma membrane reservoirs move on the cell surface towards the cleavage furrow during cytokinesis, and the plasma membrane accumulation partially persists to late cytokinesis.

A force balance model of cytokinesis

Next, we aimed to investigate how local changes in cell surface area and actin flows impact the accumulation of plasma membrane components at the cytokinetic furrow. Since it was not feasible to uncouple the individual impacts of these two factors through live cell experimentation, we opted for a modeling approach. By building on previous theoretical work (27, 28), we developed a three-dimensional biophysical model of actomyosin-driven cytokinesis, that includes the hydrodynamics of lipid flows during furrow ingression as a fundamental component (Fig. 4A, Supplementary Note 1). The model considers the cellular cortex as a thin actomyosin film that produces force and creates stresses in the cortical network (1, 29–31), and enforces force balance and mass conservation of cortex components, specifically actin and myosin. Gradients in cortical contractility ($\sigma_{\mathrm{max}}^{\mathrm{c,act}}$) drive cortical flows and cell shape changes. We assume that the cortical network behaves as an active viscous material that undergoes fast rearrangements and dissipating stresses. The cytoskeletal network is subjected to membrane-cortex adhesion, as defined by an effective membrane-cortex drag coefficient ($\gamma_{\mathrm{drag}}^{\mathrm{m-c}}$), resulting in drag forces that slow down the movement of cortex constituents. The plasma membrane behaves as a two-dimensional viscous fluid with elastic properties. Plasma membrane lipid movement is caused by cortical flows via mobile membrane-cortex protein linkers and resisted by other proteins embedded within the plasma membrane (43). We characterize the fluidity of the plasma membrane by an effective membrane lipid-protein drag coefficient ($\gamma_{\mathrm{drag}}^{\mathrm{m}}$), so that the membrane fluidity is inversely associated with the drag coefficient. Cell shape is set by the cortical configuration. Plasma membrane lipid content is quantified as a projection of lipids onto the apparent cell surface, so that a local membrane accumulation (i.e., folding) is reflected as an increased lipid density. We used experimental data from the literature to parameterize our biophysical model and numerically solved the model equations (Supplementary Note 1). Our model captured the accumulation of cortical components at the division site (Fig. S5) and reproduced the approximate cell shapes and F-actin dynamics observed in L1210 cells expressing the LifeAct F-actin sensor (Fig. S6). Thus, our model mimics the cell-intrinsic regulation of actomyosin observed during cytokinesis, thereby enabling us to investigate how the mechanical properties of the actin cortex and plasma membrane impact membrane accumulation at the furrow.

Local cell surface area compression can accumulate plasma membrane at the cytokinetic furrow

Using our biophysical model, we first examined local changes in cell shape and surface area during furrow ingression (Fig. 4B). By the end of furrow ingression, the total apparent cell surface area increased ~30% (Fig. S7). The apparent cell surface area locally compressed up to ~2.5-fold in the cytokinetic furrow and expanded up to ~10-

fold at the cell poles (Fig. 4B, Movies S2, S3). Consequently, furrow ingression alone can induce significant plasma membrane folding at the furrow, as driven by localized surface area compression, while simultaneously causing membrane unfolding at the cell poles due to local surface area expansion. We then analyzed radial and longitudinal cell surface area deformations at the cell's equator in more detail (Fig. 4C). At the onset of furrow ingression, the furrow experienced weak longitudinal compression. As furrow ingression progressed further, the furrow experienced longitudinal stretching of up to ~3-fold (Fig. 4D, Movies S2, S3). However, circumferential compression dominated over longitudinal stretching, causing an overall cell surface area compression at the furrow.

Our model enabled us to examine the mechanical factors that influence the apparent cell surface area changes at the cleavage furrow. Under high membrane-cortex adhesion, low cortical contractility, or low membrane fluidity conditions, longitudinal stretching was notably weaker than radial compression throughout furrow ingression, decreasing the apparent cell surface area at the furrow (Fig. 4F). In contrast, cells with high cortical contractility or weak membrane-cortex adhesion exhibited stronger cortical flows directed towards the cell's equator, resulting in increased accumulation of cortical material and elevated contractility at the furrow (Fig. S5). This exacerbated longitudinal stretching of the cell surface at the furrow, reducing the overall local compression of

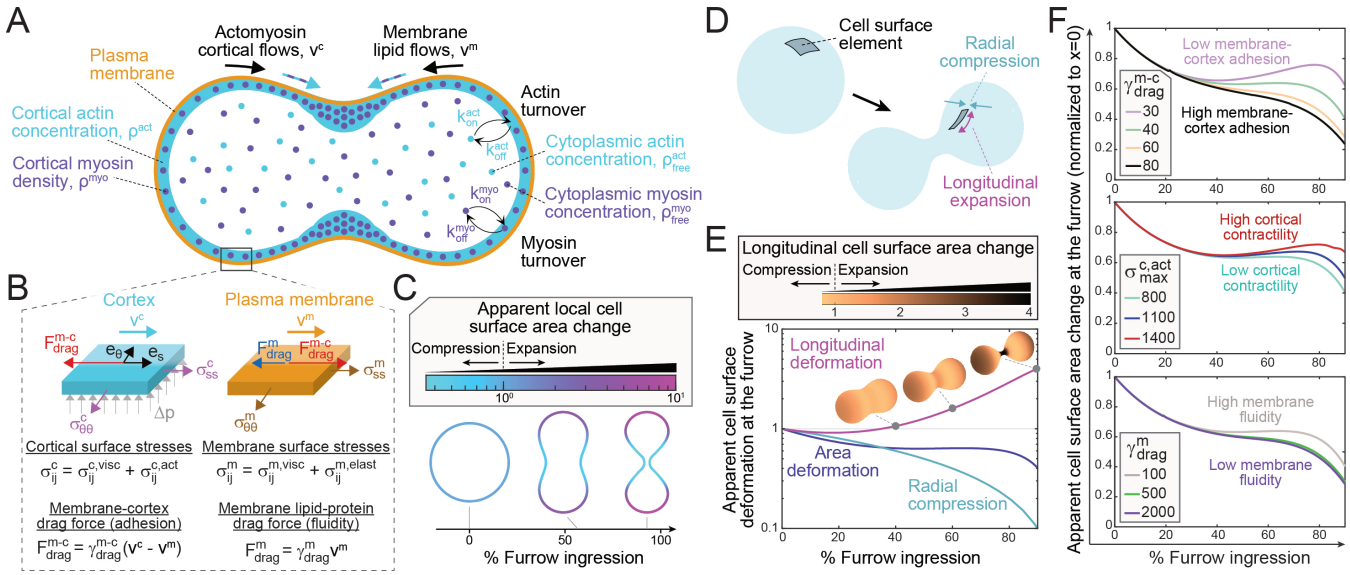

Figure 4. A force balance model of cytokinesis reveals local cell surface area changes due to radial constriction and longitudinal stretching.

(A) Schematic of the biophysical model of cytokinesis. Force balance, transport of cortical components and hydrodynamics of lipid flows during furrow ingression are fundamental components of the model. **(B)** Surface stresses and body forces on infinitesimal cortex and plasma membrane surface elements. Cortical stress forces are balanced by pressure forces and membrane-cortex adhesion forces. The cortical stress is equal to the sum of a viscous contribution $\sigma^{c,visc}_{ij}$ and an active contribution $\sigma^{c,act}_{ij} = \sigma^{c,act}_{max}\omega(\rho^{act}, \rho^{myo})g_{ij}$, where $\sigma^{c,act}_{max}$ is cortical contractility, ω is a cortex density-dependent saturating function, and i and j indicate the components of the stress tensor. Plasma membrane stress forces are balanced by drag forces. The membrane stress is the sum of viscous and elastic stresses. **(C)** Local changes in apparent cell surface area at three different timepoints during cytokinesis. **(D)** Schematic of the local changes in the apparent cell surface area due to radial and longitudinal deformations. **(E)** Apparent cell surface deformation at the cytokinetic furrow as furrow ingression progresses. Data is shown separately for apparent total area (navy), radial compression (teal), and longitudinal deformation (light purple). The cells on top depict the degree of longitudinal deformation at different locations on cell surface. **(F)** Apparent cell surface area changes at the furrow during furrow ingression for different levels of membrane-cortex adhesion (displayed in units of $pN \cdot s \cdot \mu m^{-3}$), cortical contractility (displayed in units of $pN \cdot \mu m^{-1}$), and membrane lipid-protein drag coefficient (displayed in units of $pN \cdot s \cdot \mu m^{-3}$).

the apparent cell surface area at the furrow (Fig. 4F, and Fig. S8). Overall, our results show that the apparent cell surface area experiences significant compression irrespective of the mechanical factors responsible for shaping the cell. Thus, local surface area compression promotes plasma membrane accumulation at the furrow.

Actomyosin-driven membrane flows and local surface area constriction are both responsible for the plasma membrane accumulation at the cleavage furrow

Our force balance model of cytokinesis captures the plasma membrane accumulation at the cleavage furrow (Movies S4, S5). Mechanistically, we found that high membrane fluidity and high membrane-cortex adhesion enhanced the accumulation of plasma membrane at the cleavage furrow (Fig. 5A). Interestingly, cortical contractility exhibited minimal impact on plasma membrane accumulation (Fig. 5A, *bottom*). Elevated cortical contractility resulted in a reduction in the apparent compression of cell surface at the furrow, but its effect on plasma membrane accumulation was largely cancelled out by strengthened pole-to-equator cortical flows, which also contribute to membrane accumulation at the furrow. Importantly, the modelled plasma membrane accumulation at the cleavage furrow reproduced the membrane accumulation observed in live cells (Fig. 5B), for a cortical contractility of $800\ \mathrm{pN} \cdot \mu\mathrm{m}^{-1}$, membrane-cortex drag coefficient of $30\ \mathrm{pN} \cdot \mathrm{s} \cdot \mu\mathrm{m}^{-3}$, and membrane lipid-protein drag coefficients of $100 - 200\ \mathrm{pN} \cdot \mathrm{s} \cdot \mu\mathrm{m}^{-3}$. These modeling parameters are in line with live cell measurements (29, 32–34). As exocytosis is not included in our modeling approach, these results indicate that the plasma membrane accumulation at the cleavage furrow can be explained solely by local cell surface area changes and cortex-driven membrane flows.

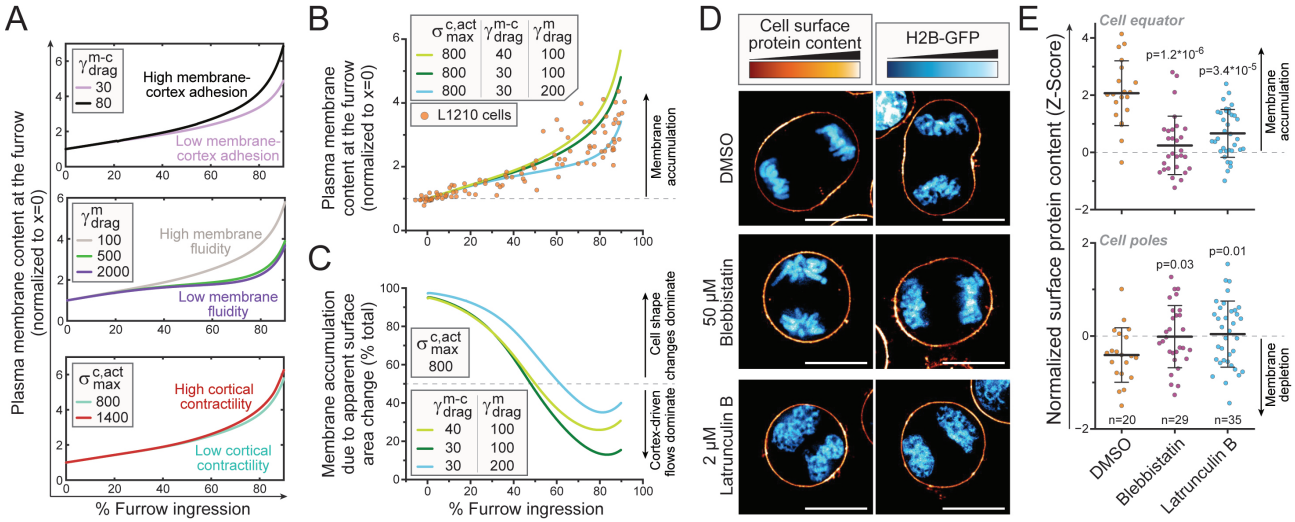

Figure 5. Actomyosin-driven membrane flows and local surface area constriction are both responsible for the plasma membrane accumulation at the cleavage furrow.
(A) Predicted plasma membrane accumulation at the furrow as furrow ingression progresses for different values of the membrane-cortex drag coefficient ($\gamma_{\mathrm{drag}}^{\mathrm{m-c}}$), membrane lipid-protein drag coefficient ($\gamma_{\mathrm{drag}}^{\mathrm{m}}$), and cortical contractility ($\sigma_{\mathrm{max}}^{\mathrm{c,act}}$). **(B)** Comparison of plasma membrane accumulation at the cytokinetic furrow in the force balance model and in live cell timelapse imaging as furrow ingression progresses. Lines depict modeling results using indicated model parameter values. Each orange dot depicts a cell at a given moment (n=14 cells with total of 103 images). **(C)** Relative contribution of apparent cell surface area changes, in comparison to cortex driven membrane flows, to the accumulation of plasma membrane at the cleavage furrow as furrow ingression progresses. **(D)** Representative images of anaphase L1210 cells expressing H2B-GFP (blue) and labeled for surface protein content (orange/yellow) after a 2 h treatment with DMSO, 50 µM (-)-Blebbistatin, or 2 µM Latrunculin B. Scale bars denote 10 µm. **(E)** Quantifications of the surface protein content at the equatorial and polar regions in the samples shown in panel (D). Lines and whiskers depict mean±SD, dots depict individual cells, n depicts the number of cells (N=2-4 independent experiments), and p-values depict comparisons to DMSO (Welch's t-test).

We then examined the relative impact that local cell surface area changes and cortex-driven membrane flows have on the accumulation of plasma membrane at the cytokinetic furrow. Using modeling parameter values that capture the membrane accumulation in live cells, we found that the local cell surface area changes and the cortex-driven membrane flows are approximately equally responsible for the membrane accumulation at the furrow (Fig. 5C). At the beginning of cleavage furrow ingression, plasma membrane accumulation at the furrow was dominated by local surface area changes, whereas cortical flows contributed more as the furrow ingression exceeded ~50% ingression (Fig. 5C). However, the degree to which local cell surface area changes were responsible for the accumulation of plasma membrane at the cytokinetic furrow was dependent on the fluidity and cortex adhesion of the plasma membrane. Local cell surface area changes dominated plasma membrane accumulation at the furrow in cells with a gel-like plasma membrane and high membrane cortex adhesion, while cortical flows emerged as the primary driving force for plasma membrane accumulation in cells with more fluid-like plasma membranes and low membrane cortex adhesion (Fig. S9A, C). Cortical contractility had only a minor influence on the relative contribution of local cell surface area changes to plasma membrane accumulation at the furrow (Fig. S9B). Overall, we conclude that plasma membrane fluidity and membrane-cortex contacts define the plasma membrane accumulation at the cleavage furrow and the predominant mechanism responsible for the membrane accumulation, whereas cortical contractility plays only a minor role. Additional regulation of the plasma membrane dynamics by anisotropic cortical contractility is detailed in Supplementary Note 2.

Finally, we validated the actomyosin-dependence of the plasma membrane dynamics. We treated L1210 cells with (-)-Blebbistatin, a non-muscle myosin II inhibitor, or Latrunculin B, an actin polymerization inhibitor, and examined plasma membrane and F-actin distributions. Treatment with both Blebbistatin and Latrunculin B prevented cytokinetic furrow ingression, the accumulation of plasma membrane and F-actin at the equatorial region, and the depletion of plasma membrane and F-actin at cell poles (Fig. 5D,E, Fig. S10). Thus, the accumulation of plasma membrane at the cytokinetic furrow is contingent upon actomyosin activity. In addition, Latrunculin B treatment caused F-actin to accumulate at random locations (Fig. S10), whereas plasma membrane protein content did not display as strong random accumulation (Fig. 5D). As Latrunculin B prevents actin polymerization, the random F-actin localization is primarily driven by cortex flows. Therefore, a local accumulation of F-actin by cortex flows is not always sufficient to drive extensive membrane accumulation at the same location.

DISCUSSION

During cytokinesis, cells undergo major mechanical deformations that result in significant structural alterations to the plasma membrane. Here, we have revealed the mechanistic basis for an extensive accumulation of plasma membrane components at the cleavage furrow and the intercellular bridge. This plasma membrane accumulation will decrease membrane tension at the cleavage furrow (20, 35) and generate a membrane tension gradient across the cytokinetic cell. The local changes in membrane accumulation and tension can impact several cellular processes. Most notably, decreased membrane tension at the intercellular bridge facilitates the recruitment of the abscission machinery and the completion of cell division (7, 9–13). We propose that the plasma membrane accumulation at the furrow acts as a mechanism to support the completion of cytokinesis. In addition, exocytosis and endocytosis can be triggered by high and low local membrane tensions, respectively (36–40). Based on membrane tension alone, exocytosis is favored at the cell poles and endocytosis at the cleavage furrow during ingression. This prediction agrees with experimental results in early cytokinesis (20, 41). The force-induced plasma membrane deformations revealed by our study could also result in localized regulation of mechanotransduction in cytokinesis (35, 42). For example, the membrane accumulation at the intercellular bridge could influence the mechanosensitive Piezo1 channel, which localizes to the intercellular bridge and controls cytokinetic abscission (43). Furthermore, our results

suggest that many of the individual membrane proteins (and lipids) that accumulate at the cleavage furrow may do so due to the general movement of the plasma membrane rather than a protein (or lipid) specific accumulation mechanism.

Our results indicate that localized exocytosis is not required for explaining the accumulation of excess plasma membrane at the cytokinetic furrow, although exocytosis is known to be required for the completion of cytokinesis (44–50). It is possible that exocytosis plays a crucial role by supplying specific components to the plasma membrane, or by secreting specific intracellular components (51). However, increasing the plasma membrane area during cytokinesis may not be required. Plasma membrane folds contain excess surface area that is estimated to be ~50%, or more, of the apparent cell surface area (52, 53), and we observed that cells arrested to prometaphase displayed a highly folded membrane structure. As the apparent cell surface area increases only ~30% during ingression, cytokinesis could proceed in the absence of plasma membrane area addition, by relying solely on the unfolding of membrane reservoirs. Thus, cytokinesis-specific increase in plasma membrane area may not be necessary for a successful cell division, especially when alternative mechanisms exist to decrease membrane tension at the intercellular bridge.

We find that the cortical surface experiences up to a four-fold increase in local longitudinal stretching at the cleavage furrow as the furrow constricts. This phenomenon is consistently observed across a wide range of modeling parameters, resulting in mechanical stresses on the plasma membrane that may hinder the completion of cytokinesis. The predicted longitudinal stretching at the furrow stands in contrast to previous studies from *C. elegans* embryos that suggested longitudinal compression at the division plane throughout furrow constriction (54, 55). This previous conclusion relied on measurements of actin cortex dynamics, which could misleadingly result in an apparent longitudinal cortical compression at the furrow as the cortical flows slowdown near the division plane. In contrast, our results uncouple local cell surface deformations from cortical flow effects, revealing simultaneous cell surface longitudinal stretching and slowdown of cortical components as they approach the division plane.

More broadly, our study focuses on, and is limited to, the cell intrinsic mechanical regulation of plasma membrane dynamics during cytokinesis. Given that the actomyosin contractile ring is a conserved feature among animal cells, we propose that the mechanisms that govern plasma membrane accumulation at the cleavage furrow are also conserved across animals. This is supported by previous observations of plasma membrane accumulation at the site of cell division in *Drosophila* neuroblasts (26). However, the degree of plasma membrane accumulation under *in vivo* conditions remains unclear, as cell-extrinsic factors, such as cell-cell and cell-substrate interactions, can impact plasma membrane and actomyosin mechanics. Other limitations of our study are detailed in Supplementary Note 3.

Overall, our work indicates that the cytoskeletal forces governing cell division simultaneously accumulate plasma membrane at the cleavage furrow and the intercellular bridge. This may serve as a self-protecting mechanism against cytokinetic failures that arise from high membrane tension. Genetic and chemical manipulations that target actomyosin or membrane-cortex adhesion, including drug treatments, may therefore impact cytokinetic fidelity indirectly by regulating plasma membrane dynamics and tension.

MATERIALS AND METHODS

Cell lines, cell culture, cell cycle reporters & chemical treatments

L1210, HeLa and BaF3 cells were cultured in RPMI (Invitrogen # 11835030) supplemented with 10% FBS (Sigma-Aldrich), 10mM HEPES, 1mM sodium pyruvate and antibiotic/antimycotic. The L1210 cells were obtained from ATCC (#CCL-219), the BaF3 cells were obtained from RIKEN BioResource Center, and the HeLa cells were gifted by the laboratory of Matthew Vander Heiden at Massachusetts Institute of Technology. All experiments were carried out with exponentially growing cells at a confluency of 300.000 – 600.000 cells/ml. All cell lines tested negative for mycoplasma.

The cell lines were transduced with a lentiviral vector carrying H2B-GFP encoding plasmid and puromycin resistance, graciously gifted by Dr Kiera M. Sapp. L1210 and BaF3 cell transductions were carried out using spinoculation in culture media containing 8 µg/ml polybrene (56). After spinoculation, the cells were resuspended in normal culture media and grown o/n. The spinoculation procedure was repeated the next day after which selection was started using 5 µg/ml of puromycin. After a week of selection, high GFP expressing cells were sorted using FACS. HeLa H2B-GFP cells were gifted by Dr. Kiera M. Sapp. L1210 cells expressing the LifeAct F-actin sensor were generated in a previous study (57).

For chemical treatments of live cells, we used DMSO (vehicle), 50 µM (-)-Blebbistatin (Cayman Chemical, Item #13013) or 2 µM Latrunculin B (Cayman Chemical, Item #10010631) for 2 hours. For live cells experiments, the chemicals were present in media during imaging.

Plasma membrane protein and lipid labeling

Plasma membrane proteins on the external side of the membrane were labelled using the LIVE/DEAD Fixable Red Dead Cell Stain kit (Invitrogen, #L23102), which labels all free amine groups. The cells were washed with ice cold PBS, mixed in ice cold PBS with the amine reactive stain. All suspension cell washes were carried out using short and weak centrifugation (1 min at 300 g), in order to minimize cell shape perturbations. Staining concentration was 5x supplier's recommended concentration. Staining was carried out in dark at +4°C for 10 minutes. Staining was stopped by mixing the cells FBS containing culture media to outcompete the amine reactive dye, after which the cells were washed once. The cells were then moved to media and imaged. For end-point imaging, this media was at +4°C, whereas for timelapse imaging this media was at +37°C. Thiol-reactive stain labeling of cell surface proteins was carried out as with the amine-reactive stain, except using Alexa Fluor 568 C5 Maleimide (Invitrogen, #A20341) at 50 µM concentration.

Plasma membrane lipids were labelled using CellMask Deep Red Plasma membrane stain (Invitrogen, # C10046). Staining concentration was 2x supplier's recommended concentration, and staining was carried out in media at RT for 10 min, followed by a wash using culture media. Plasma membrane oligosaccharides were labelled using Alexa Fluor 350 conjugate of WGA (Invitrogen, #W11263) after washing the cells with PBS. Staining concentration was 10 µg/mL, and staining was carried out in PBS in dark at +4°C for 20 minutes, followed by a was using PBS. Cells were then moved to media and imaged.

For plasma membrane cholesterol labeling, L1210 cells were washed with PBS and fixed using 4% PFA in PBS for 10 min at RT. The cells were then washed with PBS containing 5% BSA and labeled using 100 µg/ml Filipin III in PBS for 1h at RT in dark. The cells were then washed twice with PBS and imaged in PBS immediately after.

Fluorescence microscopy

For all labeling approaches, cells were imaged immediately after labeling. Live cell imaging was carried out in
330 culture media containing an additional 5% of serum, while fixed cell imaging was carried out in PBS. All samples were plated on poly-L-lysine (Sigma-Aldrich, #P8920) coated glass bottom CELLVIEW dishes (Greiner Bio-One, #627975). Imaging was carried out at RT, except for timelapse imaging which was carried out at 37°C, using DeltaVision's wide-field deconvolution microscope with standard DAPI, FITC, TRITC and APC filters. L1210 and BaF3 cells were imaged using a 100x oil-immersion objective, while HeLa cells were imaged using a 60x oil-
335 immersion objective. The immersion oil had a refractive index of 1.516 (Cargille Laboratories).

For end-point imaging, z-slices were collected with 0.25 – 0.3 µm spacing covering typically a 15 µm height. For timelapse imaging, where phototoxicity was minimized, z-slices were collected typically with a 1 µm spacing covering typically a 10 µm height. L1210 timelapse imaging was carried out every 90 sec and HeLa timelapse imaging was carried out every 60 - 150 sec. Image deconvolution was carried out using SoftWoRx 7.0.0
340 software.

Image analysis

All images were analyzed using ImageJ (version 1.53q) and MATLAB (R2023a). Dividing cells were first identified from large images with multiple cells. For each dividing cell, the z-layer with the widest cleavage furrow was cut
345 out using ImageJ. The resulting single z-slice images were analyzed using the MATLAB analysis pipeline detailed in Figure S1. For each cell, the division plane and plasma membrane were manually defined by a freehand line profile drawn using MATLAB's Image Processing and Computer Vision toolbox. To assist and speed up the tracing of the plasma membrane, the AssistedFreehand function was used to guide the freehand line profiles. To account for the higher and variable width of the plasma membrane (i.e., folding), the images were smoothed with a 15-pixel
350 x 15-pixel square kernel that locally averaged pixel intensities throughout the image. After smoothing, a single pixel wide line profile of the traced plasma membrane outline was recorded at ~4000 points, and the distance between each point and the division plane was calculated. These pixel intensities were plotted as a function of distance from the division plane, so that each side of the dividing cell is analyzed separately. The data was then interpolated, and the two sides of the cell are averaged to give one trace per cell. For the analysis in Fig 1B and 5E, images were
355 manually assigned into groups based on their cell cycle stage, as identified using the H2B-GFP marker. Pixel intensities of each cell were normalized to Z-scores, using the mean and standard deviation of the cell being analyzed. In 5E, only anaphase cells were quantified to avoid bias from late cytokinetic cells, which are present in DMSO treated but not drug treated samples. For Fig 1C, images were classified based on manual qualitative assessment. For the analysis of the timelapse images (Fig. 3D, 5B), the maximum pixel intensity at the cleavage
360 furrow and the average intensity at the cell poles were extracted from the pixel intensity vs. distance plots described above. For each cell, the timelapses were manually aligned to the onset of anaphase, and data for each cell were normalized to the average intensities observed before and at the onset of anaphase.

Scanning electron microscopy

365 Freely proliferating L1210 H2B-GFP cells in normal culture media were placed on a round cover slip coated with poly-L-lysine. The cells were given 15 min to adhere in RT. After this, the media was removed and replaced with PBS containing 2% glutaraldehyde for fixation. The cells were fixed for 30 min at RT, then washed with PBS and twice with 100 mM sodium cacodylate buffer at 4 °C. Post fixation was carried out with 1% osmium tetroxide in the sodium cacodylate buffer for 30 min at 4 °C. The cells were then rinsed 4 times with DI H2O to remove all
370 buffer and fixative, after which the cells were dehydrated with stepwise ethanol (EtOH) treatment at RT. Each step lasted 5 min and EtOH concentrations used were 35%, 45%, 50%, 65%, 70%, 85%, 95% and 100%. This was followed by 15 min treatment with 50% EtOH and 50% tetramethyl silane (TMS), another 15 min treatment with

20% EtOH and 80% TMS, and two final 5 min treatments with 100% TMS. After this, the TMS was removed, and the cells were left to dry at RT o/n.

375 Prior to imaging, the cells were sputter coated with gold for 120 s. Imaging was carried out using Zeiss Crossbeam 540 scanning electron microscope at the Peterson (1957) Nanotechnology Materials Core Facility at the Koch Institute for Integrative Cancer Research. Images were collected using a range of imaging settings, but typical imaging was carried out with 5 kV accelerating voltage, 500 pA probe current, a working distance of 8 mm, and a magnification of approximately 4000x. For all images shown in the main figures, data was collected with a
380 resolution of 4 nm/pixel. For other images, resolution ranged from 4 to 10 nm/pixel. Images were analyzed using ImageJ (version 1.53q).

Biophysical modeling of cytokinesis

The cytokinesis numerical code was implemented in Fortran 90, while the analysis of the model outcomes was
385 conducted using MATLAB. Supplementary Table 1 provides a summary of the parameter values utilized in all the numerical simulations, unless otherwise noted. A comprehensive description of the model can be found in the Supplementary Note 1.

Data and code availability

390 All quantifications are shown in figures. The MATLAB code used for image analysis can be found at https://github.com/alicerlam/lam-miettinen-cell-membrane-intensity. All imaging data and codes used for biophysical model of cytokinesis are available at a reasonable request.

395 **ACKNOWLEDGMENTS**

This work was supported by the Koch Institute Support (core) Grant P30-CA14051 from the National Cancer Institute and by the Virginia and D.K. Ludwig Fund for Cancer Research (T.P.M.), as well as by grants U54CA210190, P01CA254849 and U54CA268069 from the National Institutes of Health (R.A.M.). We thank Prof. S. Manalis, Prof. D. J. Odde, and Prof. P. P. Provenzano for their support and mentoring, Ms. K. Suarez for technical
400 assistance, and Dr. Kiera M. Sapp for providing research materials. We also thank the Koch Institute's Robert A. Swanson (1969) Biotechnology Center, specifically the Microscopy Core Facility and the Peterson (1957) Nanotechnology Materials Core Facility and their excellent staff, for technical support.

Conflict of interest

405 The authors declare no conflict of interest.

Author contributions

R.A.M. developed and carried out the computational simulations of cytokinesis. A.L. developed the image analysis pipeline and quantified the microscopy data. T.P.M. conceived and supervised the study and carried out all imaging
410 experiments. R.A.M. and T.P.M. wrote the manuscript with assistance from A.L.

REFERENCES

1. P. Chugh, E. K. Paluch, The actin cortex at a glance. *J Cell Sci* **131** (2018).
2. U. S. Eggert, T. J. Mitchison, C. M. Field, Animal Cytokinesis: From Parts List to Mechanisms. *Annu Rev Biochem* **75**, 543–566 (2006).
3. R. A. Green, E. Paluch, K. Oegema, Cytokinesis in Animal Cells. *Annual Review of Cell and Developmental Biology* **28**, 29–58 (2012).
4. T. D. Pollard, B. O'Shaughnessy, Molecular Mechanism of Cytokinesis. *Annu Rev Biochem* **88**, 661–689 (2019).
5. B. Mierzwa, D. W. Gerlich, Cytokinetic abscission: molecular mechanisms and temporal control. *Dev Cell* **31**, 525–538 (2014).
6. F. A. Barr, U. Gruneberg, Cytokinesis: placing and making the final cut. *Cell* **131**, 847–860 (2007).
7. C. L. Stoten, J. G. Carlton, ESCRT-dependent control of membrane remodelling during cell division. *Semin Cell Dev Biol* **74**, 50–65 (2018).
8. S. M. A. Lens, R. H. Medema, Cytokinesis defects and cancer. *Nat Rev Cancer* **19**, 32–45 (2019).
9. V. Andrade, *et al.*, Caveolae promote successful abscission by controlling intercellular bridge tension during cytokinesis. *Sci Adv* **8**, eabm5095 (2022).
10. J. Lafaurie-Janvore, *et al.*, ESCRT-III assembly and cytokinetic abscission are induced by tension release in the intercellular bridge. *Science* **339**, 1625–1629 (2013).
11. V. Andrade, A. Echard, Mechanics and regulation of cytokinetic abscission. *Front Cell Dev Biol* **10**, 1046617 (2022).
12. M. R. Pavlin, J. H. Hurley, The ESCRTs – converging on mechanism. *J Cell Sci* **133** (2020).
13. V. Mercier, *et al.*, Endosomal membrane tension regulates ESCRT-III-dependent intra-lumenal vesicle formation. *Nat Cell Biol* **22**, 947–959 (2020).
14. T. D. Pollard, Nine unanswered questions about cytokinesis. *Journal of Cell Biology* **216**, 3007–3016 (2017).
15. R. G. Fehon, A. I. McClatchey, A. Bretscher, Organizing the cell cortex: the role of ERM proteins. *Nat Rev Mol Cell Biol* **11**, 276–287 (2010).
16. J. Saarikangas, H. Zhao, P. Lappalainen, Regulation of the actin cytoskeleton-plasma membrane interplay by phosphoinositides. *Physiol. Rev.* **90**, 259–289 (2010).
17. A. P. Sagona, *et al.*, PtdIns(3)P controls cytokinesis through KIF13A-mediated recruitment of FYVE-CENT to the midbody. *Nat Cell Biol* **12**, 362–371 (2010).
18. I. Kouranti, M. Sachse, N. Arouche, B. Goud, A. Echard, Rab35 regulates an endocytic recycling pathway essential for the terminal steps of cytokinesis. *Current Biology* **16**, 1719–1725 (2006).
19. K. Emoto, H. Inadome, Y. Kanaho, S. Narumiya, M. Umeda, Local change in phospholipid composition at the cleavage furrow is essential for completion of cytokinesis. *Journal of Biological Chemistry* **280**, 37901–37907 (2005).
20. J. A. Castillo-Badillo, A. C. Bandi, S. Harlalka, N. Gautam, SRRF-Stream Imaging of Optogenetically Controlled Furrow Formation Shows Localized and Coordinated Endocytosis and Exocytosis Mediating Membrane Remodeling. *ACS Synth Biol* **9**, 902–919 (2020).
21. K. Gowrishankar, *et al.*, Active remodeling of cortical actin regulates spatiotemporal organization of cell surface molecules. *Cell* **149**, 1353–1367 (2012).
22. S. Saha, *et al.*, Active emulsions in living cell membranes driven by contractile stresses and transbilayer coupling. *Proc Natl Acad Sci U S A* **119**, e2123056119 (2022).
23. G. Kunduri, U. Acharya, J. K. Acharya, Lipid Polarization during Cytokinesis. *Cells* **11**, 3977 (2022).
24. R. Raghupathy, *et al.*, Transbilayer Lipid Interactions Mediate Nanoclustering of Lipid-Anchored Proteins. *Cell* **161**, 581–594 (2015).
25. H. De Belly, *et al.*, Cell protrusions and contractions generate long-range membrane tension propagation. *Cell* **186**, 3049-3061.e15 (2023).
26. B. LaFoya, K. E. Prehoda, Actin-dependent membrane polarization reveals the mechanical nature of the neuroblast polarity cycle. *Cell Rep* **35**, 109146 (2021).

27. A. Mietke, F. Jülicher, I. F. Sbalzarini, Self-organized shape dynamics of active surfaces. *Proc Natl Acad Sci U S A* **116**, 29–34 (2019).
28. G. Salbreux, F. Jülicher, Mechanics of active surfaces. *Phys Rev E* **96**, 032404 (2017).
29. J. Y. Tinevez, *et al.*, Role of cortical tension in bleb growth. *Proc Natl Acad Sci U S A* **106**, 18581–18586 (2009).
30. T. M. Svitkina, Actin Cell Cortex: Structure and Molecular Organization. *Trends Cell Biol* **30**, 556–565 (2020).
31. P. Chugh, *et al.*, Actin cortex architecture regulates cell surface tension. *Nat Cell Biol* **19**, 689–697 (2017).
32. E. Fischer-Friedrich, A. A. Hyman, F. Jülicher, D. J. Müller, J. Helenius, Quantification of surface tension and internal pressure generated by single mitotic cells. *Sci Rep* **4**, 1–8 (2014).
33. A. X. Cartagena-Rivera, J. S. Logue, C. M. Waterman, R. S. Chadwick, Actomyosin Cortical Mechanical Properties in Nonadherent Cells Determined by Atomic Force Microscopy. *Biophys J* **110**, 2528–2539 (2016).
34. A. E. Cohen, Z. Shi, Do Cell Membranes Flow Like Honey or Jiggle Like Jello? *BioEssays* **42**, 1900142 (2020).
35. A. L. Le Roux, X. Quiroga, N. Walani, M. Arroyo, P. Roca-Cusachs, The plasma membrane as a mechanochemical transducer. *Philosophical Transactions of the Royal Society B* **374** (2019).
36. N. C. Gauthier, M. A. Fardin, P. Roca-Cusachs, M. P. Sheetz, Temporary increase in plasma membrane tension coordinates the activation of exocytosis and contraction during cell spreading. *Proc Natl Acad Sci U S A* **108**, 14467–14472 (2011).
37. M. M. Kozlov, L. V. Chernomordik, Membrane tension and membrane fusion. *Curr Opin Struct Biol* **33**, 61–67 (2015).
38. G. Wang, T. Galli, Reciprocal link between cell biomechanics and exocytosis. *Traffic* **19**, 741–749 (2018).
39. J. Dai, H. Ping Ting-Beall, M. P. Sheetz, The Secretion-coupled Endocytosis Correlates with Membrane Tension Changes in RBL 2H3 Cells. *J Gen Physiol* **110**, 1 (1997).
40. M. Staykova, D. P. Holmes, C. Read, H. A. Stone, Mechanics of surface area regulation in cells examined with confined lipid membranes. *Proc Natl Acad Sci U S A* **108**, 9084–9088 (2011).
41. B. Feng, H. Schwarz, S. Jesuthasan, Furrow-Specific Endocytosis during Cytokinesis of Zebrafish Blastomeres. *Exp Cell Res* **279**, 14–20 (2002).
42. X. Quiroga, *et al.*, A mechanosensing mechanism controls plasma membrane shape homeostasis at the nanoscale. *Elife* **12** (2023).
43. J. Carrillo-Garcia, *et al.*, The mechanosensitive Piezo1 channel controls endosome trafficking for an efficient cytokinetic abscission. *Sci Adv* **7**, 7785–7814 (2021).
44. J. A. Schiel, *et al.*, FIP3-endosome-dependent formation of the secondary ingression mediates ESCRT-III recruitment during cytokinesis. *Nat Cell Biol* **14**, 1068–1078 (2012).
45. J. A. Schiel, *et al.*, Endocytic membrane fusion and buckling-induced microtubule severing mediate cell abscission. *J Cell Sci* **124**, 1411–1424 (2011).
46. J. W. Goss, D. K. Toomre, Both daughter cells traffic and exocytose membrane at the cleavage furrow during mammalian cytokinesis. *Journal of Cell Biology* **181**, 1047–1054 (2008).
47. A. Gromley, *et al.*, Centriolin anchoring of exocyst and SNARE complexes at the midbody is required for secretory-vesicle-mediated abscission. *Cell* **123**, 75–87 (2005).
48. J. K. Schweitzer, E. E. Burke, H. V Goodson, C. D'Souza-Schorey, Endocytosis resumes during late mitosis and is required for cytokinesis. *Journal of Biological Chemistry* **280**, 41628–41635 (2005).
49. C. B. Shuster, D. R. Burgess, Targeted new membrane addition in the cleavage furrow is a late, separate event in cytokinesis. *Proc Natl Acad Sci U S A* **99**, 3633–3638 (2002).
50. G. M. Wilson, *et al.*, The FIP3-Rab11 protein complex regulates recycling endosome targeting to the cleavage furrow during late cytokinesis. *Mol Biol Cell* **16**, 849–860 (2005).
51. T. P. Miettinen, K. S. Ly, A. Lam, S. R. Manalis, Single-cell monitoring of dry mass and dry mass density reveals exocytosis of cellular dry contents in mitosis. *Elife* **11** (2022).
52. L. Guillou, *et al.*, T-lymphocyte passive deformation is controlled by unfolding of membrane surface reservoirs. *Mol Biol Cell* **27**, 3574–3582 (2016).

53. G. W. Schmid-Schonbein, Y. Y. Shih, S. Chien, Morphometry of Human Leukocytes. *Blood* **56**, 866–875 (1980).
54. R. N. Khaliullin, *et al.*, A positive-feedback-based mechanism for constriction rate acceleration during cytokinesis in Caenorhabditis elegans. *Elife* **7** (2018).
55. A. C. Reymann, F. Staniscia, A. Erzberger, G. Salbreux, S. W. Grill, Cortical flow aligns actin filaments to form a furrow. *Elife* **5** (2016).
56. J. H. Kang, *et al.*, Monitoring and modeling of lymphocytic leukemia cell bioenergetics reveals decreased ATP synthesis during cell division. *Nat Commun* **11**, 4983 (2020).
57. J. H. Kang, *et al.*, Noninvasive monitoring of single-cell mechanics by acoustic scattering. *Nat Methods* **16**, 263–269 (2019).